# Many-body quantum theory of the optical parametric oscillator

C. J. Mertens and T. A. B. Kennedy
*School of Physics, Georgia Institute of Technology, Atlanta, Georgia 30332-0430*

S. Swain
*Department of Applied Mathematics and Theoretical Physics, The Queen's University of Belfast, Belfast BT7 1NN, Northern Ireland*
(Received 16 February 1993)

A many-body theory of quantum fluctuations in the optical parametric oscillator is given. Dyson equations and diagrammatic representation of photon Green functions are derived from a combination of quantum Langevin and many-body techniques. Single-photon Green functions are used to compute dynamic spectra of the output using a self-consistent scheme which incorporates nonlinear, many-photon polarization effects. The latter scale with system size and their influence on the nonlinear quantum dynamics is addressed. We present results of dynamic output spectra and quantum-noise properties beyond the adiabatic approximation.

PACS number(s): 42.50.Lc, 42.50.Dv, 05.30.Jp

## I. INTRODUCTION

The quantum statistical properties of electromagnetic fields produced by nonlinear mixing processes in dissipative cavity systems are now quite well understood in the *semiclassical limit* of nearly coherent fields. The observation of squeezed states of light falls into this category [1], and theories based on a linearization of quantum fluctuations around the classical Maxwell field accurately describe the dynamics [2]. In order to produce strongly quantum-dynamical behavior the coherent coupling of field and matter must be significantly increased. Efforts are underway to achieve this *quantum limit* in cavity quantum electrodynamics using the resonant interaction of atoms in an optical cavity [3]. Technological advances in the construction of monolithic cavities [4], and cavities with ultrahigh-reflectivity mirrors [5], suggest that it may eventually be possible to investigate the quantum limit in other nonlinear optical systems, though this will also depend on the availability of materials with large nonlinearity and low absorption. The theoretical treatment of such nonlinear quantum dynamics is difficult because linearization theory breaks down, and a more sophisticated analysis is necessary. This is true also in the vicinity of a nonequilibrium phase transition where fluctuation effects are generically large.

Here we present a nonlinear quantum-dynamical analysis of the degenerate optical parametric oscillator (OPO). Earlier theoretical investigations of this system have appeared [6,7]. The transition from the semiclassical to quantum limits was studied in the adiabatic limit by Wolinsky and Carmichael [7] and Reid and Yurke [7], who discussed coherent-state superpositions and mixtures, while quantum tunneling rates between metastable states were computed by Kinsler and Drummond [7].

The quantum noise in a dissipative system has an intrinsic scale, the system-size parameter. In the case of an OPO, this parameter is physically the number of intracavity pump photons required to reach the oscillation threshold $n_{\rm th}$. Clearly, if $n_{\rm th} \gg 1$, as is commonly the case, the quantum noise is a small perturbation to the classical dynamics; this is the semiclassical limit. If $n_{\rm th}$ is reduced, the quantum noise grows, and new physics is to be expected in the quantum limit. Reduction of $n_{\rm th}$ is achieved by increasing the operating-frequency medium nonlinearity and cavity $Q$, and reducing the cavity-mode volume to provide tight confinement [8]. In this regime the OPO presents the possibility for investigation of quantum dissipative phenomena far from thermal equilibrium. In addition to nonlinear optical systems, Josephson-junction parametric amplifiers are good candidates for observation of system-size effects, since the intrinsic nonlinearity is large [9].

The quantum limit is theoretically challenging because of the need to treat the dynamics nonperturbatively in the following sense. If one regards the classical Maxwell-field analysis as zeroth order, and linearized quantum theory as first-order perturbation theory in the inverse system-size parameter, then in the quantum limit we must in principle sum the perturbation series to high or infinite order. Ideally one hopes for a technique that allows physical insight into the nonlinear quantum fluctuations, or *many-body* photon processes, as well as presenting a systematic method for the calculation of the observables of photodetection-based experiments. Here we present a many-body nonequilibrium Green-function approach, which fulfills both of these criteria [10–13]. The method was partially outlined by Zaidi [14], though we go considerably further here in developing a self-consistent scheme. Certain discrepancies between Ref. [14] and the present work will be pointed out in the following. We have confirmed that our results are in agreement with those known from adiabatic theory in the appropriate limit [6]. With suitable definitions, the Green functions are themselves spectral quantities observed in power and homodyne spectral measurements. One advantage of Green functions is that, with the aid of diagrammatic techniques, they allow a nonperturbative (in

 

the sense discussed above), self-consistent formulation. The diagrams themselves help considerably towards an understanding of the nature of the nonlinear photon-scattering processes, which are significant in the quantum limit. They also present an interesting alternative perspective on the phase-dependent squeezing in an OPO. Although Green-function methods have been applied in some contexts to quantum radiation problems [12], systematic application through self-consistent perturbation theory has not. This alone is significant, because of the limitations of other techniques [15].

Here we outline the application of the many-body method to the OPO by deriving the basic equations analytically from the familiar standpoint of the quantum Langevin equations. While this is useful as an introduction, in practice diagrammatic methods alone can be used to write down the Dyson equations, i.e., the equations satisfied by one-particle or one-photon Green functions. These are then solved numerically by self-consistent iteration to convergence. To the previously uninitiated it is helpful to see the diagrams derived analytically. The basic Feynman rules and diagram topology can be found by a few orders of interaction-picture perturbation theory.

The remainder of this paper is organized as follows. In Sec. II the basic theory of the OPO and the generating functional for nonequilibrium Green functions are introduced. In Sec. III we derive the Dyson equations for the familiar linearized theory (semiclassical limit), which predicts perfect quadrature squeezing at threshold. In Sec. IV we treat the quantum many-body phenomena neglected by the linearized theory and show how these scale with system size. A useful approximation associated with the bare vertex is discussed in Sec. V. Results of some applications of the technique are given in Sec. VI, and our conclusions are summarized in Sec. VII. In Appendices A and B we discuss the application of Wick's theorem and list some useful identities and symmetry relations for the Green functions.

## II. BACKGROUND THEORY

### A. Optical parametric oscillator

The OPO comprises two discrete optical cavity modes, the subharmonic and pump, which interact due to the presence of a nonlinear intracavity crystal with effective nonlinearity $\kappa$ [16–18]. The nonlinearity enables pump photons with frequency $\omega_2=2\omega_1$ to split into two subharmonic photons of frequency $\omega_1$, and vice versa. The pump is driven by a resonant external field, and both modes are damped due to loss through the cavity mirrors. This enables a nonthermal equilibrium to be established.

Although our subsequent analysis does not use the reduced density matrix explicitly, it is useful to introduce the notation and transformations on the master equation. We begin by considering the OPO master equation given by Drummond, McNeil, and Walls [6], in the rotating frame with both modes at resonance

$$\frac{d\rho}{dt}=\frac{\kappa}{2}[a_1^{\dagger 2}a_2-a_2^{\dagger}a_1^2,\rho]+\epsilon_2[a_2^{\dagger}-a_2,\rho] + \sum_{k=1}^{2}\gamma_k\{2a_k\rho a_k^{\dagger}-a_k^{\dagger}a_k\rho-\rho a_k^{\dagger}a_k\}\ , \tag{2.1}$$

where $\rho$ is the density operator, $a_k$ and $a_k^{\dagger}$ ($k=1,2$) are annihilation and creation operators for the modes, $\kappa$ is the nonlinearity, $\epsilon_2$ is the pump driving field, and $\gamma_k$ ($k=1,2$) are the mode damping rates. Below threshold the subharmonic (mode 1) has zero mean value and the pump (mode 2), which is driven by the external field $\epsilon_2$, has mean amplitude $\alpha_2$ determined by the steady-state classical equations. A unitary transformation with the coherent-state displacement operator $D(\alpha_2)$ is performed on Eq. (2.1), using $D(\alpha_2)^{\dagger}a_2D(\alpha_2)=a_2+\alpha_2$, so that the subharmonic and pump operators have zero mean value in the vacuum picture. The transformed master equation is given by

$$\frac{d\hat{\rho}}{d\tau}=\frac{1}{i\hbar}[H_1+H_2,\hat{\rho}] + \sum_{k=1}^{2}\frac{\gamma_k}{\gamma_1}\{2a_k\hat{\rho}a_k^{\dagger}-a_k^{\dagger}a_k\hat{\rho}-\hat{\rho}a_k^{\dagger}a_k\}\ , \tag{2.2}$$

where $\hat{\rho}$ is the transformed density operator, $\tau=\gamma_1 t$ is time measured in units of the inverse damping rate $\gamma_1^{-1}$ of the subharmonic mode 1, and the Hamiltonians are defined by

$$H_1=i\hbar\frac{p}{2}[a_1^{\dagger 2}-a_1^2]\ , \qquad H_2=i\hbar\frac{1}{2\sqrt{n_{\rm th}}}[a_1^{\dagger 2}a_2-a_1^2a_2^{\dagger}]\ . \tag{2.3}$$

Here $p$, the normalized pump parameter, is proportional to the pump laser amplitude $\epsilon_2$. It varies in the range $0\le p\le 1$, between zero pumping and threshold. The system-size parameter $n_{\rm th}$ corresponds physically to the intracavity pump photon number at threshold. In terms of the parameters of Eq. (2.1), $n_{\rm th}=(\gamma_1/\kappa)^2$ and $p=\kappa\epsilon_2/\gamma_1\gamma_2$. At threshold the subharmonic undergoes a phase transition and attains a nonzero amplitude. Above threshold an additional Hamiltonian term proportional to this amplitude must be included in Eq. (2.2). Here we will consider only the region below threshold.

### B. External currents, path ordering, and Green functions

Following the method introduced by Schwinger [10,19], we add a Hamiltonian perturbation [12],

$$H_J^{\zeta}(t)=i\hbar\sum_{k=1}^{2}[J_k^{\zeta}(t)a_k^{\dagger}(t)-J_k^{\zeta *}(t)a_k(t)]\ , \tag{2.4}$$

where $J_k^{\zeta}(t)$, $k=1,2$, are prescribed classical currents and $t$ is understood to represent the dimensionless time introduced in Eq. (2.2). The currents are introduced as a formal device to enable correlation functions to be generated by functional differentiation, and are finally set to zero to obtain physical results. The index $\zeta=+$ or $-$, labels the four orderings of two Heisenberg operators that can be

generated by this method, as we now describe. From the two Heisenberg picture operators $A(t)$ and $B(t')$, we may construct the correlation functions $\langle T(A(t)B(t'))\rangle$, $\langle \tilde{T}(A(t)B(t'))\rangle$, $\langle A(t)B(t')\rangle$, and $\langle B(t')A(t)\rangle$, where $T$ and $\tilde{T}$ are Dyson's time- and antitime-ordering operators, respectively. The time-ordered function may be visualized as arising from the operator ordering on a contour directed in the positive sense ($\zeta=+$) along the time axis. Similarly the antitime-ordered function corresponds to the ordering of operators on a contour directed in the negative sense ($\zeta=-$). To incorporate all four correlation functions into a single prescription, Keldysh [11] considered a contour running along the upper lip ($\zeta=+$) of the time axis in the positive sense, turning around at a distant future time, and returning along the lower lip ($\zeta=-$) of the contour in the negative sense; see Fig. 1. Time arguments are considered to be displaced onto the upper or lower lip, according to which correlation one wishes to consider. Explicitly,

$$\begin{aligned}
&\langle T(A(t)B(t'))\rangle=\langle T_C(A(t_+)B(t'_+))\rangle ,\\
&\langle \tilde{T}(A(t)B(t'))\rangle=\langle T_C(A(t_-)B(t'_-))\rangle ,\\
&\langle A(t)B(t')\rangle=\langle T_C(A(t_-)B(t'_+))\rangle ,\\
&\langle B(t')A(t)\rangle=\langle T_C(A(t_+)B(t'_-))\rangle ,
\end{aligned} \tag{2.5}$$

where $T_C$ is the path-ordering operator along the contour of Fig. 1.

We now turn to the Green functions. First we define the generating functional [12]

$$F[J]=\exp\left[\sum_{\zeta}\sum_{k}\zeta\int_{-\infty}^{\infty}dt\,[J_k^{\zeta}(t)a_k^{\dagger}(t)-J_k^{\zeta *}(t)a_k(t)]\right] . \tag{2.6}$$

Thus we have, for example,

$$\begin{aligned}
\langle a_k^{\dagger}(t)\rangle&=\lim_{J\to 0}\langle a_k^{\dagger}(t_{\zeta})\rangle_J\equiv\lim_{J\to 0}\frac{1}{\zeta}\frac{\delta}{\delta J_k^{\zeta}(t)}\ln\langle T_C(F[J])\rangle\\
&=\lim_{J\to 0}\frac{\langle T_C(a_k^{\dagger}(t_{\zeta})F[J])\rangle}{\langle T_C(F[J])\rangle} .
\end{aligned} \tag{2.7}$$

The $J_k^{\zeta}(t)$ and $J_k^{\zeta}(t)^*$ are treated as independent functions for the purpose of functional differentiation, and we append an index to the operator time argument to take care of the path ordering. Second functional derivatives generate the Green functions, which are of two types, propagator Green functions $D_k^{\zeta\zeta'}(t,t')$ and anomalous Green functions $\mathfrak{D}_k^{\zeta\zeta'}(t,t')$, and are defined as

$$\begin{aligned}
iD_k^{\zeta\zeta'}(t,t')&=\langle T_C(a_k^{\dagger}(t_{\zeta}),a_k(t'_{\zeta'}))\rangle ,\\
\mathfrak{D}_k^{\zeta\zeta'}(t,t')&=\langle T_C(a_k(t_{\zeta}),a_k(t'_{\zeta'}))\rangle ,
\end{aligned} \tag{2.8}$$

$k=1,2$, where we use the notation $\langle T_C(A,B)\rangle=\langle T_C(AB)\rangle-\langle T_C(A)\rangle\langle T_C(B)\rangle$. If one considers Heisenberg equations, or quantum Langevin equations in the case of an open system, for the single-time averages $\langle a_i^{\dagger}(t)\rangle_J$ in the presence of external currents, equations of motion for the Green functions may be found by functional differentiation using identities such as

$$\begin{aligned}
\lim_{J\to 0}\left[-\frac{1}{\beta}\frac{\delta}{\delta J_k^{\beta}(t')}\langle a_k^{\dagger}(t_{\alpha})\rangle_J\right]&=\langle T_C(a_k^{\dagger}(t_{\alpha}),a_k(t'_{\beta}))\rangle\\
&=iD_k^{\alpha\beta}(t,t') .
\end{aligned} \tag{2.9}$$

## III. LINEARIZED THEORY OF QUANTUM FLUCTUATIONS

### A. Derivation of the Dyson equations

The input-output theory of Gardiner and Collett [20] shows that a Markovian master equation theory, in the rotating-wave approximation, may alternatively be cast in the form of quantum Langevin equations in which the input noise terms have simple causal properties. Applied to the OPO master equation described in Sec. II A, one finds the subharmonic satisfies the quantum Langevin equation

$$\begin{aligned}
\frac{d}{dt}a_1^{\dagger}(t)=&-a_1^{\dagger}(t)+pa_1(t)+\frac{1}{\sqrt{n_{\rm th}}}a_2^{\dagger}(t)a_1(t)\\
&+J_1^{\beta *}(t)-\sqrt{2}a_{1,\rm in}^{\dagger}(t) ,
\end{aligned} \tag{3.1}$$

where $\beta=+$ or $-$, $a_{1,\rm in}^{\dagger}(t)$ is the free input noise operator, with zero mean (the cavity driving is already accounted for in the coefficient $p$) and free field commutator $[a_{1,\rm in}(t),a_{1,\rm in}^{\dagger}(t')]=\delta(t-t')$. If we take expectation values of Eq. (3.1) in the presence of the external current and functionally differentiate with respect to $J_1^{\beta *}(t')$, according to (2.9) this brings down a factor $[-\beta a_1(t'_{\beta})]$ inside the path-ordering operator. Then taking the limit as $J\to 0$ one finds equations of motion for the physical propagator Green functions of the subharmonic mode. An identical procedure performed on the Hermitian conjugate to Eq. (3.1) yields equations for the anomalous Green functions.

For simplicity we first consider the linearized theory of quantum fluctuations in the OPO. This has received a good deal of attention as it predicts perfect quadrature squeezing in one quadrature of the subharmonic at the oscillation threshold. Here we recover the standard results from an alternative perspective, and correct some previous results of Zaidi [14]. However, we wish to stress that the power of the many-body approach lies not in an elegant reproduction of well-known results, but in presenting a path towards an understanding of nonlinear

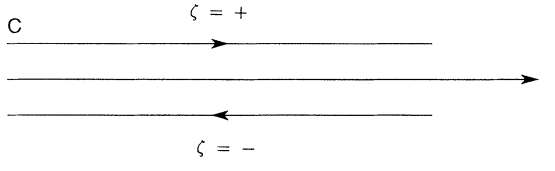


FIG. 1. The contour $C$ on which the path-ordering operator $T_C$ is defined. Operator time arguments are considered to be displaced onto the upper or lower branch.

quantum fluctuations. This is considered in subsequent sections.

The linearized theory is found by dropping the nonlinear term in Eq. (3.1). Formally, this is justified in the limit of $n_{\rm th}\to\infty$. The Green functions obey the equations

$$\frac{d}{dt}D_1^{\alpha\beta}(t,t')=-D_1^{\alpha\beta}(t,t')-ip\mathfrak{D}_1^{\alpha\beta}(t,t')+i\beta\delta(t-t') +\sqrt{2}i\langle T_C(a_{1,\rm in}^\dagger(t_\alpha),a_1(t'_\beta))\rangle , \quad (3.2)$$

$$\frac{d}{dt}\mathfrak{D}_1^{\alpha\beta}(t,t')=-\mathfrak{D}_1^{\alpha\beta}(t,t')+ipD_1^{\alpha\beta}(t,t') -\sqrt{2}i\langle T_C(a_{1,\rm in}(t_\alpha),a_1(t'_\beta))\rangle . \quad (3.3)$$

The input-internal correlations that appear may be simplified by using the causal relations [20]

$$[c(t'),a_{1,\rm in}(t)]=-\sqrt{2}\Theta(t'-t)[c(t'),a_1(t)] ,$$
$$[c(t'),a_{1,\rm in}^\dagger(t)]=-\sqrt{2}\Theta(t'-t)[c(t'),a_1^\dagger(t)] , \quad (3.4)$$

where $c(t)$ is an arbitrary system operator and $\Theta(t)$ is the Heaviside step function. Using these relations we may simplify Eqs. (3.3) to the matrix form

$$\left[\frac{d}{dt}+1\right]\underline{D}_1(t,t')=-ip\underline{\mathfrak{D}}_1(t,t')-\underline{\Lambda}\,\underline{D}_1(t,t') +i\underline{\sigma}_3\delta(t-t') , \quad (3.5)$$

$$\left[\frac{d}{dt}+1\right]\underline{\mathfrak{D}}_1(t,t')=ip\underline{D}_1(t,t')-\underline{\Xi}\,\underline{\mathfrak{D}}_1(t,t') ,$$

where

$$\underline{D}_k(t,t')=\begin{bmatrix}D_k^{++}(t,t') & D_k^{+-}(t,t')\\ D_k^{-+}(t,t') & D_k^{--}(t,t')\end{bmatrix} \quad (3.6)$$

and similarly for $\underline{\mathfrak{D}}_1$; $\underline{\sigma}_3=\mathrm{diag}(1,-1)$ is the third Pauli matrix, and the damping matrices are given by

$$\underline{\Lambda}=2\begin{bmatrix}-1 & 1\\ 0 & 0\end{bmatrix} , \quad \underline{\Xi}=2\begin{bmatrix}0 & 0\\ 1 & -1\end{bmatrix} . \quad (3.7)$$

As we are interested in steady-state properties, we Fourier-transform Eqs. (3.5) using time translation invariance $f(t,t')=f(t-t')$,

$$[\underline{\Lambda}+(1-i\omega)\hat{\underline{1}}]\underline{D}_1(\omega)=-ip\underline{\mathfrak{D}}_1(\omega)+i\underline{\sigma}_3 ,$$
$$[\underline{\Xi}+(1-i\omega)\hat{\underline{1}}]\underline{\mathfrak{D}}_1(\omega)=ip\underline{D}_1(\omega) , \quad (3.8)$$

where $\hat{\underline{1}}$ is the unit matrix, and the Fourier transform is defined as

$$D_i^{\xi\xi'}(\omega)=\int_{-\infty}^{\infty}d\tau\, e^{i\omega\tau}D_i^{\xi\xi'}(t+\tau,t) , \quad (3.9)$$

with $\omega$ the frequency offset from resonance in units of $\gamma_1$. In the absence of interaction $p=0$, we can identify the empty-cavity-propagator Green functions (indicated by a caret)

$$\hat{\underline{D}}_1^{-1}(\omega)=-i\underline{\sigma}_3[\underline{\Lambda}+(1-i\omega)\hat{\underline{1}}]$$
$$\Rightarrow\hat{\underline{D}}_1(\omega)=\begin{bmatrix}\dfrac{1}{-\omega+i} & \dfrac{-2i}{(\omega+i)(\omega-i)}\\ 0 & \dfrac{1}{\omega+i}\end{bmatrix} . \quad (3.10)$$

A similar analysis for the pump mode gives the empty-cavity propagator $\hat{\underline{D}}_2(\omega)$, which is identical with the matrix (3.10) upon making the replacement $i\to i\gamma$ everywhere, where $\gamma=\gamma_2/\gamma_1$ is the ratio of the pump to subharmonic cavity decay rates.

Since $[\underline{\Xi}+(1-i\omega)\hat{\underline{1}}]=-i\underline{\sigma}_3(\hat{\underline{D}}_1^{-1}(-\omega))^T$, where superscript $T$ denotes real transpose, Eqs. (3.8) may be written

$$\underline{D}_1(\omega)=\hat{\underline{D}}_1(\omega)+\hat{\underline{D}}_1(\omega)(-p\underline{\sigma}_3)\underline{\mathfrak{D}}_1(\omega) ,$$
$$\underline{\mathfrak{D}}_1(\omega)=(\hat{\underline{D}}_1(-\omega))^T(-p\underline{\sigma}_3)\underline{D}_1(\omega) . \quad (3.11)$$

Equations (3.11) are the Dyson equations for the linearized theory. These may be represented graphically as shown in Fig. 2. A coupling between propagator and anomalous Green functions is familiar in the quantum theory of Bose gases [21]. However, in that case the coupling arises from scattering processes involving the Bose condensate. For the OPO the intracavity pump-field amplitude plays the symmetry-breaking role. The latter is nonzero as a consequence of external driving rather than

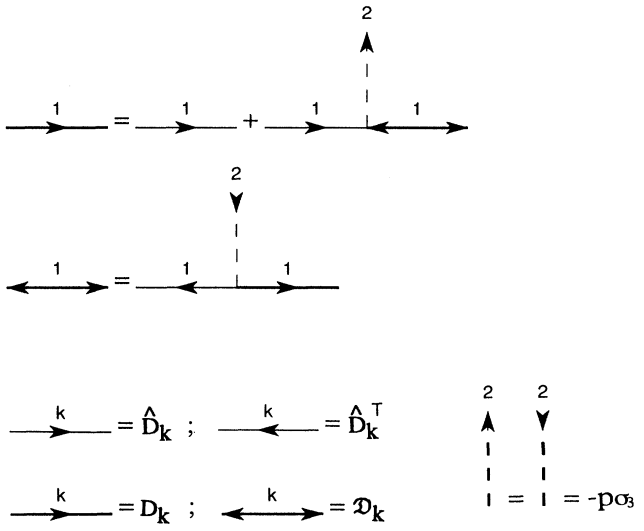


FIG. 2. Diagrammatic representation of subharmonic-mode Dyson equations for the linearized theory. All lines directed from left to right and two-way directed lines are Green-function matrices as a function of $\omega$. Lines directed from right to left are the transpose of Green-function matrices as a function of $-\omega$. Thin and thick directed lines represent empty-cavity and linearized propagator matrices, respectively, while the anomalous propagator matrix is represented by a two-way directed line. The mean pump field, given by a dashed line, has one free end. Vertices represent parametric scattering processes involving two subharmonic photons and the pump mean field, and matrix multiplication is implied as defined in Eq. (3.11).

condensation. Superconductivity is another example where a condensed phase plays a qualitatively important role. The attraction between electrons at the Fermi surface binds electrons of opposite spin in a Cooper pair. These constitute a condensate with nonzero amplitude, given by the pair wave function or Ginzburg-Landau order parameter. The resulting Gor'kov equations for superconductivity have a similar topology to Fig. 2 [21,22], though the Green-function lines are interpreted as matrices in the nonequilibrium approach presented here. The physics is also quite different. In superconductivity the pair wave function is proportional to the superconducting energy gap, the threshold energy required to break a Cooper pair, and is associated with the real part of the Green-function poles in the complex $\omega$ plane. In the OPO, the pump amplitude determines the distance to the oscillation threshold, and this is manifest in the lifetimes, or widths, of the squeezed and antisqueezed quadrature fluctuations, i.e., the imaginary part of the Green-function poles, $\omega = i(1 \pm p)$.

An alternative diagrammatic view is useful, which emphasizes the parametric nature of the scattering processes. We introduce the self-energy matrix [14,21]

$$\underline{\Sigma}_1(\omega) = \underline{\hat{D}}_1^{-1}(\omega) - \underline{D}_1^{-1}(\omega) , \tag{3.12}$$

which accounts for the energy shifts and lifetime modifications of the elementary excitations (damped cavity photons) due to the parametric scattering from the mean pump field. The Dyson equation $\underline{D}_1(\omega) = \underline{\hat{D}}_1(\omega) + \underline{\hat{D}}_1(\omega)\underline{\Sigma}(\omega)\underline{D}_1(\omega)$ then follows from Eqs. (3.11) and (3.12), with

$$\underline{\Sigma}_1(\omega) = p^2 \underline{\sigma}_3 \underline{\hat{D}}_1^{T}(-\omega)\underline{\sigma}_3 , \tag{3.13}$$

and is illustrated in Fig. 3. The picture of repeated parametric interactions between subharmonic photons and the mean pump amplitude arises in a natural way.

### B. Quadrature fluctuation spectrum

The spectrum of output quadrature fluctuations of the subharmonic with respect to unit shot noise is given by

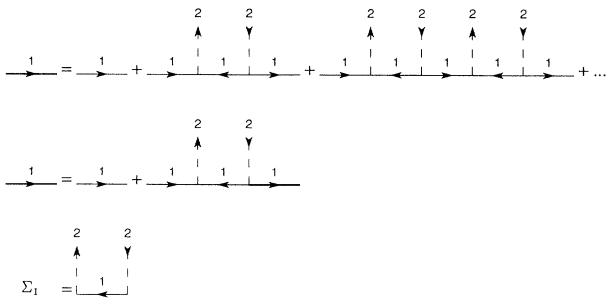

FIG. 3. Alternative diagrammatic representation of the propagator in terms of the self-energy $\underline{\Sigma}_1(\omega)$ in linearized theory. Intracavity subharmonic photons are repeatedly scattered from the mean pump field. These interactions are incorporated in the self-energy as shown.

$$\begin{aligned} V(X_{1\pm},\omega) &= \int_{-\infty}^{\infty} d\tau\, e^{i\omega\tau} \langle X_{1\pm}(t+\tau), X_{1\pm}(t) \rangle \\ &= 1 + 2\{ iD_1^{-+}(\omega) + iD_1^{-+}(-\omega) \\ &\quad \pm 2\,\mathrm{Re}[\mathfrak{D}_1^{++}(\omega)]\} , \end{aligned} \tag{3.14}$$

where $X_{1+} = a_{1,\mathrm{out}} + a_{1,\mathrm{out}}^{\dagger}$ and $X_{1-} = (a_{1,\mathrm{out}} - a_{1,\mathrm{out}}^{\dagger})/i$ are the output amplitude and phase quadrature operators. The output operators $a_{1,\mathrm{out}}$ and $a_{1,\mathrm{out}}^{\dagger}$ are free fields that obey the commutator $[a_{1,\mathrm{out}}(t), a_{1,\mathrm{out}}^{\dagger}(t')] = \delta(t-t')$. From the Dyson equations (3.11) it follows that

$$\begin{aligned} iD_1^{-+}(\omega) &= \frac{2p^2}{[\omega^2 + (1-p)^2][\omega^2 + (1+p)^2]} , \\ \mathfrak{D}_1^{++}(\omega) &= \frac{p(\omega^2 + 1 + p^2)}{[\omega^2 + (1-p)^2][\omega^2 + (1+p)^2]} , \end{aligned} \tag{3.15}$$

and thus we find the well-known spectrum of quadrature fluctuations [1]

$$V(X_{1\pm},\omega) = 1 \pm \frac{4p}{\omega^2 + (1 \mp p)^2} , \tag{3.16}$$

with perfect squeezing of the $-$ quadrature and divergence of the $+$ quadrature at threshold $p = 1$. We note that the propagator and anomalous Green functions, defined in terms of the internal interacting field operators, determine the observable spectrum directly. Proper account of the boundary condition at the output mirror has been made in deriving Eqs. (3.14)–(3.16) by using the relation $a_{1,\mathrm{out}}(t) - a_{1,\mathrm{in}}(t) = \sqrt{2}a_1(t)$ between output, input, and internal fields. Equation (3.14) also corrects an expression given by Zaidi [14]. The optical spectrum is given by $2iD_1^{-+}(\omega)$ directly. Integration of $(V(X_{1\pm},\omega) - 1)$ and $iD_1^{-+}(\omega)$ over all frequencies gives the steady-state normally ordered intracavity variance in quadrature fluctuations and subharmonic photon number, respectively,

$$\begin{aligned} \langle :(\Delta X_{1\pm})^2: \rangle &= \frac{1}{4\pi} \int_{-\infty}^{\infty} d\omega (V(X_{1\pm},\omega) - 1) , \\ \langle n_1 \rangle &= \frac{1}{2\pi} \int_{-\infty}^{\infty} d\omega\, iD_1^{-+}(\omega) + |\alpha_1|^2 . \end{aligned} \tag{3.17}$$

For the linearized theory we find

$$\begin{aligned} \langle :(\Delta X_{1\pm})^2: \rangle &= \pm p/(1 \mp p) , \\ \langle n_1 \rangle &= p^2/[2(1-p^2)] , \end{aligned}$$

where : : denotes normal ordering. The definitions (3.14) and (3.17) are also applicable in the nonlinear quantum limit.

## IV. NONLINEAR THEORY: MANY-BODY GREEN FUNCTIONS AND DYSON EQUATIONS

If we do not assume the limit of infinite system size $n_{\mathrm{th}} = \infty$ in Eq. (3.1), but proceed to the derivation of Eqs. (3.2) and (3.3) as before, we find extra nonlinear contributions, the many-body Green functions. These are familiar from the analysis of many-body phenomena in condensed-matter physics [21] and in quantum electrodynamics [19]. They are typically simplified into sums of

products of one-body Green functions and vertex corrections, by means of Wick's theorem [21,22]. We reserve a brief discussion of the latter to Appendix A.

### A. Propagator Green functions

We first consider the nonlinear corrections to the propagator Green-function equation. This leads to the additional contribution

$$\frac{-i}{\sqrt{n_{\rm th}}}\langle T_C(a_2^\dagger(t_\alpha)a_1(t_\alpha),a_1(t'_\beta))\rangle$$

on the right-hand side of Eq. (3.2). In the steady state, where $\langle a_1(t)\rangle=0$, it is sufficient to consider only $\langle T_C(a_2^\dagger(t_\alpha)a_1(t_\alpha)a_1(t'_\beta))\rangle$. Following standard many-body theory [21], we analyze the many-body Green function with unequal time arguments

$$iG_{\alpha\beta}(t_1,t_2;t_3)\equiv\frac{1}{\sqrt{n_{\rm th}}}\langle T_C(a_2^\dagger(t_{1\alpha})a_1(t_{2\alpha})a_1(t_{3\beta}))\rangle\ , \tag{4.1}$$

where all operators are in the Heisenberg picture. To proceed we transform to the interaction picture, in which the operators evolve according to the (Hamiltonian) cavity-reservoir coupling and the states according to the intracavity Hamiltonian interactions. Equation (4.1) is then written

$$iG_{\alpha\beta}(t_1,t_2;t_3)=\frac{1}{\sqrt{n_{\rm th}}}\langle T_C(S\hat{a}_2^\dagger(t_{1\alpha})\hat{a}_1(t_{2\alpha})\hat{a}_1(t_{3\beta}))\rangle\ , \tag{4.2}$$

where a caret denotes interaction picture operators and

$$S=T_C\left\{\exp\left[-\frac{i}{\hbar}\sum_\zeta\zeta\int_{-\infty}^{\infty}dt[H_1(t)+H_2(t)]\right]\right\} \tag{4.3}$$

is the path-ordered $S$ matrix. We now proceed through a perturbative expansion of $S$, using Wick's theorem to simplify the multiple-time correlation functions.

To zeroth order $S=1$, $G_{\alpha\beta}^{(0)}=0$, since an equal number of annihilation and creation operators is a minimum requirement for a nonzero result. To first order, only $H_2$ produces a contribution

$$\begin{aligned}iG_{\alpha\beta}^{(1)}(t_1,t_2;t_3)&=\frac{1}{2n_{\rm th}}\sum_\mu\mu\int_{-\infty}^{\infty}dt_\mu\langle T_C(\hat{a}_1^\dagger(t_\mu)\hat{a}_1^\dagger(t_\mu)\hat{a}_2(t_\mu)\hat{a}_2^\dagger(t_{1\alpha})\hat{a}_1(t_{2\alpha})\hat{a}_1(t_{3\beta}))\rangle\\&=\frac{1}{n_{\rm th}}\sum_\mu\mu\int_{-\infty}^{\infty}dt_\mu[i\hat{D}_2^{\alpha\mu}(t_1,t_\mu)][i\hat{D}_1^{\mu\alpha}(t_\mu,t_2)][i\hat{D}_1^{\mu\beta}(t_\mu,t_3)]\ ,\end{aligned} \tag{4.4}$$

where Wick's theorem is used in the second line and carets on Green functions denote empty-cavity propagators as in Eq. (3.10). The diagrammatic representation of (4.4) is instructive, and is shown in Fig. 4(a). Continuing the perturbation series to higher order we find additional contributions which represent corrections to the empty-cavity Green functions [lines in Fig. 4(a)], plus other terms which represent corrections to the bare vertex of Fig. 4(a). To all orders in perturbation theory the Green functions are fully renormalized, and the vertex function is the set of all diagrams that can be connected to one incoming mode-2 line and two outgoing mode-1 lines, excluding those diagrams that merely represent corrections to the incoming and outgoing lines themselves. We represent this mathematically by

$$iG_{\alpha\beta}(t_1,t_2;t_3)=\frac{1}{n_{\rm th}}\sum_\mu\mu_1\mu_2\mu_3\int_{-\infty}^{\infty}d\tau_1d\tau_2d\tau_3[iD_2^{\alpha\mu_1}(t_1,\tau_1)][iD_1^{\mu_2\alpha}(\tau_2,t_2)][iD_1^{\mu_3\beta}(\tau_3,t_3)]\Gamma^{\mu_1\mu_2\mu_3}(\tau_1,\tau_2,\tau_3) \tag{4.5}$$

and diagrammatically in Fig. 4(b), with $\Gamma$ the vertex part.

From time translation invariance the three-time correlation function and the vertex part are functions of two independent time differences, and since we may write $\omega_1\tau_1+\omega_2\tau_2+\omega_3\tau_3=\omega_1(\tau_1-\tau_3)+\omega_2(\tau_2-\tau_3)+\tau_3(\omega_1+\omega_2+\omega_3)$, it follows that

$$2\pi\delta(\omega_1+\omega_2+\omega_3)\Gamma^{\mu_1\mu_2\mu_3}(\omega_1,\omega_2,-(\omega_1+\omega_2))=\int_{-\infty}^{\infty}d\tau_1d\tau_2d\tau_3e^{i(\omega_1\tau_1+\omega_2\tau_2+\omega_3\tau_3)}\Gamma^{\mu_1\mu_2\mu_3}(\tau_1,\tau_2,\tau_3)\ , \tag{4.6}$$

with a similar relation for $G_{\alpha\beta}(\omega_1,\omega_2;-(\omega_1+\omega_2))$. In frequency space Eq. (4.5) becomes

$$iG_{\alpha\beta}(\omega_1,\omega_2;-(\omega_1+\omega_2))=\frac{1}{n_{\rm th}}\sum_\mu\mu_1\mu_2\mu_3[iD_2^{\alpha\mu_1}(\omega_1)][iD_1^{\mu_2\alpha}(-\omega_2)][iD_1^{\mu_3\beta}(\omega_1+\omega_2)]\Gamma^{\mu_1\mu_2\mu_3}(\omega_1,\omega_2,-(\omega_1+\omega_2))\ . \tag{4.7}$$

The Dyson equation for the propagator is modified from Eq. (3.11) to

$$\underline{D}_1(\omega)=\underline{\hat{D}}_1(\omega)+\underline{\hat{D}}_1(\omega)(-p\underline{\sigma}_3)\underline{\mathfrak{D}}_1(\omega)+\frac{1}{2\pi}\int_{-\infty}^{\infty}d\omega_1\underline{\hat{D}}_1(\omega)(-i\underline{\sigma}_3)\underline{G}(\omega_1,\omega-\omega_1;-\omega)\ . \tag{4.8}$$

The diagrammatic representation of this equation is given in Fig. 5.

### B. Anomalous Green functions

The procedure is the same as in Sec. IV A. The three-point Green function that arises from the nonlinear coupling term is, by analogy with Eq. (4.1),

$$ig_{\alpha\beta}(t_1,t_2;t_3)=\frac{1}{\sqrt{n_{\rm th}}}\langle T_C(a_1^\dagger(t_{1\alpha})a_2(t_{2\alpha})a_1(t_{3\beta}))\rangle \ . \tag{4.9}$$

Again, this is evaluated perturbatively by transforming to the interaction picture, expanding the $S$ matrix in powers of the interactions, and using Wick's theorem to perform the contractions. The lowest nonvanishing contribution arises from a cross term between $H_1$ and $H_2$ at second order, which yields

$$ig^{(1)}_{\alpha\beta}(t_1,t_2;t_3)=\frac{1}{n_{\rm th}}\sum_\mu \int_{-\infty}^{\infty} dt_\mu [i\hat{D}_1^{\alpha\mu}(t_1,t_\mu)] \times [i\hat{D}_2^{\mu\alpha}(t_\mu,t_2)] \times [\hat{\mathfrak{D}}_1^{\mu\beta}(t_\mu,t_3)] \ . \tag{4.10}$$

Then, introducing a vertex function $\Upsilon$, by arguments similar to those in Sec. IV A, the fully renormalized three-time function may be written in Fourier space as

$$ig_{\alpha\beta}(\omega_1,\omega_2;-(\omega_1+\omega_2))=\frac{1}{n_{\rm th}}\sum_\mu \mu_1\mu_2\mu_3[iD_1^{\alpha\mu_1}(\omega_1)][iD_2^{\mu_2\alpha}(-\omega_2)][\mathfrak{D}_1^{\mu_3\beta}(\omega_1+\omega_2)]\Upsilon^{\mu_1\mu_2\mu_3}(\omega_1,\omega_2,-(\omega_1+\omega_2)) \ . \tag{4.11}$$

The full nonlinear Dyson equation in frequency space then follows as

$$\underline{\mathfrak{D}}_1(\omega)=\underline{\hat{D}}_1^T(-\omega)(-p\underline{\sigma}_3)\underline{D}_1(\omega) + \frac{1}{2\pi}\int_{-\infty}^{\infty} d\omega_1 \underline{\hat{D}}_1^T(-\omega)(-\underline{\sigma}_3)\underline{g}(\omega_1,\omega-\omega_1;-\omega) \ . \tag{4.12}$$

The diagrammatic representation of Eq. (4.12) is given in Fig. 6.

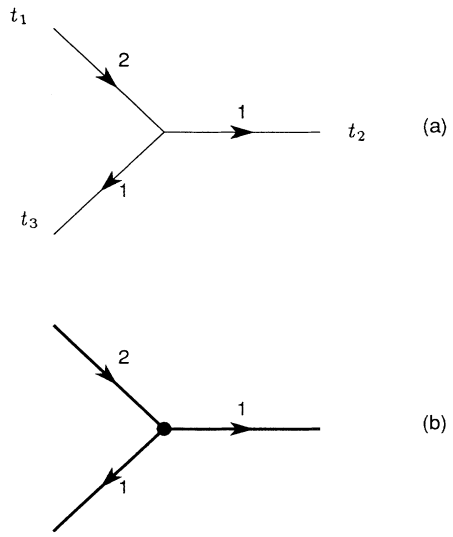


FIG. 4. (a) Vertex representing the lowest nonvanishing contribution to the many-body Green function, in terms of the empty-cavity Green-function lines. The vertex represents a parametric scattering of two subharmonic photons and one pump photon. (b) Fully renormalized many-body Green function. The empty-cavity propagators are replaced by exact propagators, and the bare vertex is replaced by a vertex part, indicated by the solid circle.

## V. BARE-VERTEX APPROXIMATION

### A. Analysis

A relatively simple closed form set of Dyson equations for the propagator and anomalous Green-function matrices follows in the bare-vertex approximation. That is when the vertex functions $\Gamma$ and $\Upsilon$ are replaced by their lowest-order contributions, which are of order unity, and independent of system size $n_{\rm th}$. The higher-order corrections all involve a mode-2 Green-function line, proportional to $1/n_{\rm th}$. Provided $n_{\rm th}$ is not of order unity or smaller, it is reasonable to drop these corrections. A similar simplification with, however, a different physical origin arises in the theory of electron-phonon interactions, and is known as Migdal's theorem [21]. Many-body effects are retained self-consistently and summed to infinite order in the exact Green-function lines.

In the bare vertex approximation the vertex functions are given by

$$\Gamma^{\mu_1\mu_2\mu_3}(\omega_1,\omega_2,-(\omega_1+\omega_2))=\Upsilon^{\mu_1\mu_2\mu_3}(\omega_1,\omega_2,-(\omega_1+\omega_2)) =\delta^{\mu_1\mu_2}\delta^{\mu_3\mu_2} \ . \tag{5.1}$$

This result is substituted into Eqs. (4.8) and (4.12) to give

$$\underline{D}_1(\omega)=\underline{\hat{D}}_1(\omega)+\underline{\hat{D}}_1(\omega)(-p\underline{\sigma}_3)\underline{\mathfrak{D}}_1(\omega) +\underline{\hat{D}}_1(\omega)\underline{\Pi}_1(\omega)\underline{D}_1(\omega) \ , \tag{5.2}$$

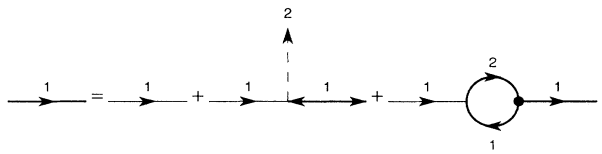


FIG. 5. Dyson equation for the propagator including quantum fluctuations of the pump. The exact propagator has three contributions: (1) the empty-cavity propagator, (2) renormalization through repeated parametric scattering from the mean pump field, and (3) repeated quantum parametric scattering from pump photons. The intracavity pump field enters in both *condensate* and *noncondensate* phases.

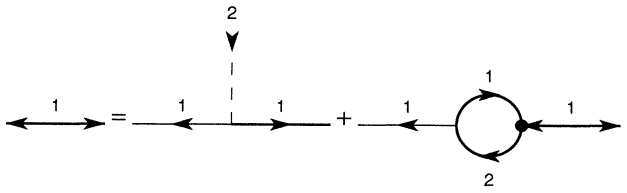


FIG. 6. Dyson equation for the anomalous propagator including quantum fluctuations of the pump, illustrating the repeated parametric scattering from pump mean field (condensate) and pump photons (noncondensate).

$$\underline{\mathfrak{D}}_1(\omega)=\hat{\underline{D}}_1^{T}(-\omega)(-p\underline{\sigma}_3)\underline{D}_1(\omega) + \hat{\underline{D}}_1^{T}(-\omega)\underline{\Pi}_1^{T}(-\omega)\underline{D}(\omega) , \tag{5.3}$$

where the polarization function $\underline{\Pi}_1$ is defined by an integral of exact Green functions [14]

$$\Pi_1^{\alpha\beta}(\omega)=\frac{i}{2\pi n_{\rm th}}\alpha\beta\int_{-\infty}^{\infty}d\omega_1 D_2^{\alpha\beta}(\omega_1)D_1^{\beta\alpha}(\omega_1-\omega) \tag{5.4}$$

and is represented by a bubble diagram. To determine the "exact" pump Green function $\underline{D}_2$ appearing in (5.4), we need the corresponding Dyson equation. This is given, in the bare-vertex approximation (see Fig. 7), by

$$\underline{D}_2(\omega)=\hat{\underline{D}}_2(\omega)+\hat{\underline{D}}_2(\omega)\underline{\Pi}_2(\omega)\underline{D}_2(\omega) , \tag{5.5}$$

where $\Pi_2$, the polarization function for the pump mode, satisfies the convolution integral

$$\Pi_2^{\alpha\beta}(\omega)=\frac{i}{2\pi n_{\rm th}}\alpha\beta\int_{-\infty}^{\infty}d\omega_1 D_1^{\alpha\beta}(\omega_1)D_1^{\alpha\beta}(\omega-\omega_1) . \tag{5.6}$$

Another way to write result (5.3) is to introduce the partially renormalized Green function $\tilde{\underline{D}}_1(\omega)$ [14], for which $\underline{\Pi}_1$ is the self-energy, i.e.,

$$\underline{\Pi}_1(\omega)=\hat{\underline{D}}_1^{-1}(\omega)-\tilde{\underline{D}}_1^{-1}(\omega) . \tag{5.7}$$

Equation (5.3) may then be written in the form

$$\underline{\mathfrak{D}}_1(\omega)=\tilde{\underline{D}}_1^{T}(-\omega)(-p\underline{\sigma}_3)\underline{D}_1(\omega) . \tag{5.8}$$

### B. Numerical methods

The Dyson equations are coupled nonlinear integral equations in frequency space. The important simplifying feature is that the polarization functions (5.6) and (5.7) are convolution integrals and may be computed from known Green functions quickly and efficiently by using fast-Fourier-transform (FFT) methods. The self-consistent solution of the Dyson equations is initiated at a given operating point $p$ by computing the polarization functions from the linearized Green functions via FFT. The polarization functions are, in turn, used to update the Green functions according to Eqs. (5.2) and (5.3). This procedure is then repeated until convergence is obtained. The relations listed in Appendix B may be used to check the numerics.

Since the linearized Green functions diverge at threshold, they do not provide a useful starting point for the self-consistent solution in the immediate vicinity of threshold. However, it is possible instead to initiate the iteration scheme using the converged Green functions from a nearby operating point, and simultaneously improve the convergence rate. In this way the threshold may be approached from below or above, using the linearized Green function to start the procedure outside the threshold region.

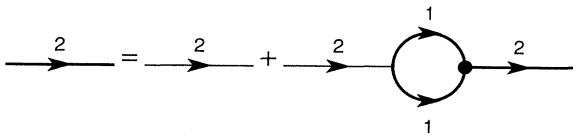


FIG. 7. Dyson equation for the pump-mode (noncondensate) propagator. Diagrams represent the empty-cavity propagator and subharmonic induced polarization via repeated parametric scattering.

## VI. RESULTS

In this section we wish to illustrate several points: (1) The many-body approach produces results in agreement with the coherent-state adiabatic theories [5–8]. The comparison is made by frequency integration of the steady-state Green functions obtained by the self-consistent solution of the Dyson equations (5.2)–(5.6), with the adiabatic parameter $\gamma=\gamma_2/\gamma_1\gg 1$. (2) The many-body approach goes well beyond the adiabatic theory in two respects. First, since $\gamma$ is arbitrary we are not restricted to the adiabatic limit. In the adiabatic limit the system-size scaling arises only in the combination $n_{\rm th}\,\gamma$. Secondly, the theory is a *dynamical* one since observable spectra are found directly in terms of Green functions. By contrast, adiabatic theory provides an explicit solution for the steady-state quasiprobability distribution, and this only allows the calculation of single-time averages. In principle, stochastic simulation can be used to yield dynamical results, but this procedure has so far proved difficult to implement in nonlinear quantum problems, adiabatic or otherwise.

In Fig. 8 the intracavity photon number versus pump parameter $p$ is shown in the adiabatic limit $\gamma=100$ and $n_{\rm th}=10$, and is compared with the adiabatic theory of Ref. [5]. The linearized theory, for which the photon number diverges at threshold, is also shown for comparison. Here the Dyson equations (5.2)–(5.6) are iterated to convergence for each $p$, and the converged Green functions integrated according to Eq. (3.17). The smooth dependence of photon number with pumping shown in Fig. 8 indicates how system-size quantum fluctuations have an important role in smoothing out the nonequilibrium phase transition predicted by the classical theory, for which the photon number is identically zero below $p=1$.

Monolithic resonators with $n_{\rm th}$ as low as $10^6$–$10^7$ have been employed in the laboratory [23]. It is possible that with careful design this could be reduced by a few orders

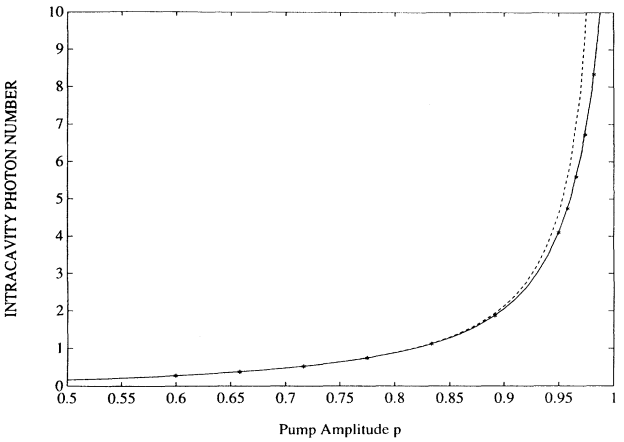


FIG. 8. Comparison of the intracavity subharmonic photon number vs pump parameter $p$ for the adiabatic complex $P$-function method (solid line), the Green-function method (*), and linearized theory (— — —). The oscillator threshold is at $p=1$. Parameters are $\gamma=100$, $n_{\rm th}=10$. Marked deviations from linearized theory are apparent near threshold where it diverges.

of magnitude, e.g., by increasing pump frequency, cavity $Q$, and medium nonlinearity (without increasing intracavity absorption) and reducing the mode volume. Note, however, that reducing mode volume by decreasing the cavity length reduces the light round-trip time, and thus the cavity $Q$. New materials, or any method of obtaining large nonlinearity with low loss, are potentially important in approaching the quantum limit in the optical domain. However, Josephson-junction parametric oscillators which have a higher intrinsic nonlinearity than nonresonant optical processes are more promising candidates for investigations of the quantum limit at this time.

The many-body approach enables investigation of the scaling behavior which distinguishes the quantum and semiclassical regimes. In Figs. 9(a) and 9(b) this is illustrated by showing the zero-frequency quadrature fluctuations of the subharmonic mode as a function of $n_{\rm th}$. The operating point is arbitrarily fixed at 95% ($p=0.95$) of threshold throughout, and $\gamma=1$, well outside the adiabatic limit. Quadrature noise is independent of $n_{\rm th}$ in the semiclassical limit, and thus system-size effects become significant below $n_{\rm th}\approx 10^5$. Closer to threshold, $1>p>0.95$, one expects scaling to set in at higher values of $n_{\rm th}$. In addition, Fig. 9(c) illustrates the convergence of the self-consistent scheme for the antisqueezing quadrature and $n_{\rm th}=48.3$. We note that at each order of iteration classes of diagrams are summed to all orders in $n_{\rm th}$ and this greatly improves the convergence properties.

In Fig. 10(a) we show the spectrum of squeezing for three values of $n_{\rm th}$ from Fig. 9, representing the semiclassical limit, the transition region, and the quantum limit, respectively. As expected, the squeezing is reduced in the quantum limit, due to the many-body parametric scattering of subharmonic and pump photons. Notice also the emergence of a central peak in the spectrum for $n_{\rm th}=48.3$, as indicated in Fig. 10(b). This phenomena becomes even more pronounced when the nonadiabatic limit is probed further. Figure 11(a) shows the squeezing spectrum for $\gamma=0.1$ and $n_{\rm th}=600$, 1000, 10 000, and $\infty$. Note that the many-body processes polarize both the subharmonic and pump modes. The influence of pump

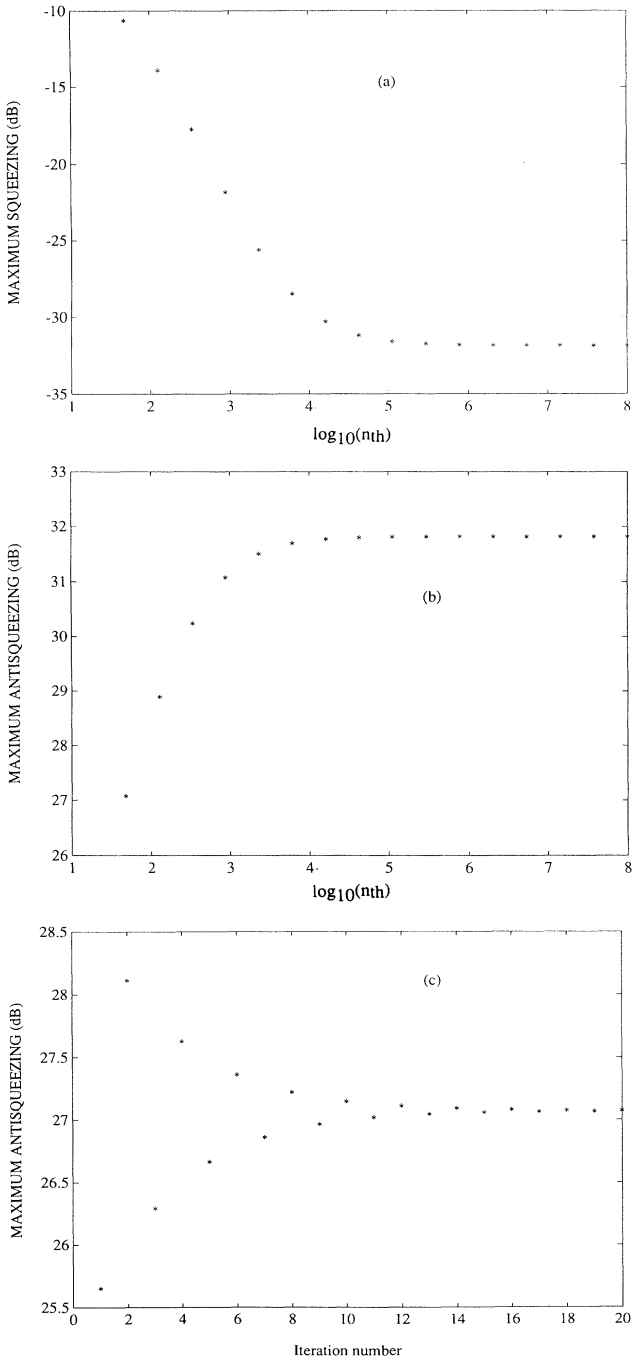


FIG. 9. System-size scaling for the zero-frequency component of the output quadrature fluctuation spectra, at 95% of threshold ($p=0.95$), $\gamma=1$, for (a) the squeezed quadrature, (b) the antisqueezed quadrature, and (c) the convergence of the antisqueezing quadrature for $n_{\rm th}=48.3$.

polarization has a quantitative effect on the data shown. We confirmed this by comparing the data obtained by setting the pump polarization to zero in Eq. (5.5) and recalculating the subharmonic Green functions self-consistently, as illustrated in Fig. 11(b) for $n_{\rm th}=600$. This is one of the advantages available to the many-body approach. The diagrams enhance physical insight and enable the role of particular many-body processes to be evaluated quantitatively.

## VII. CONCLUSIONS

We have developed a self-consistent many-body Green-function approach for the study of quantum dynamics beyond the semiclassical limit. For the parametric oscillator the quantum limit is characterized by large quantum fluctuations and small photon numbers. A small number of pump photons is required to reach oscillation threshold, precluding a semiclassical understanding of the system behavior. The pictorial advantages of the diagrammatic approach enable a clear delineation of the scattering processes at work in the semiclassical and quantum limits: quadrature squeezing, a semiclassical phenomenon, is due to repeated parametric scattering of subharmonic photons from the mean pump field, or "condensate." In the quantum limit polarization of the pump and subharmonic modes due to repeated parametric scattering involving the pump "noncondensate" becomes increasingly important. The quantum limit may be investigated through the system-size scaling behavior these processes introduce.

Our approach goes beyond earlier theories of the OPO in two essential respects: (1) It enables phenomena outside of the adiabatic limit $\gamma_2 \gg \gamma_1$ to be studied, and (2) like the tunneling-time calculations of Refs. [5,7], it provides fully *quantum dynamical* results. Earlier work related to single-time observables only, while we compute spectral information directly. The method may obviously be applied to other quantum optical phenomena. It is still an open question whether intracavity nonlinear optics, based on off-resonant processes, will enable the quantum limit to be achieved experimentally. Resonant intracavity excitation of atoms in cavity quantum electro-

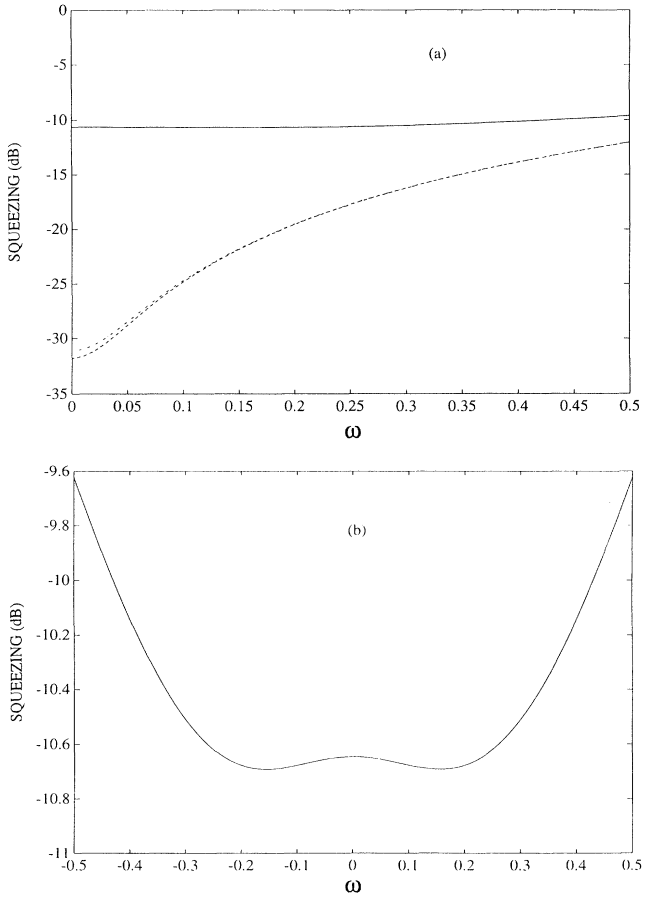


FIG. 10. Spectrum of squeezing at 95% of threshold ($p=0.95$), $\gamma=0.1$, for (a) $n_{\rm th}=48.3$ (solid line), $4.28\times10^4$ (dash-dotted line), and $2.1\times10^6$ (dashed line), and (b) $n_{\rm th}=48.3$. Note a half-range scale is used in (a) for the sake of clarity.

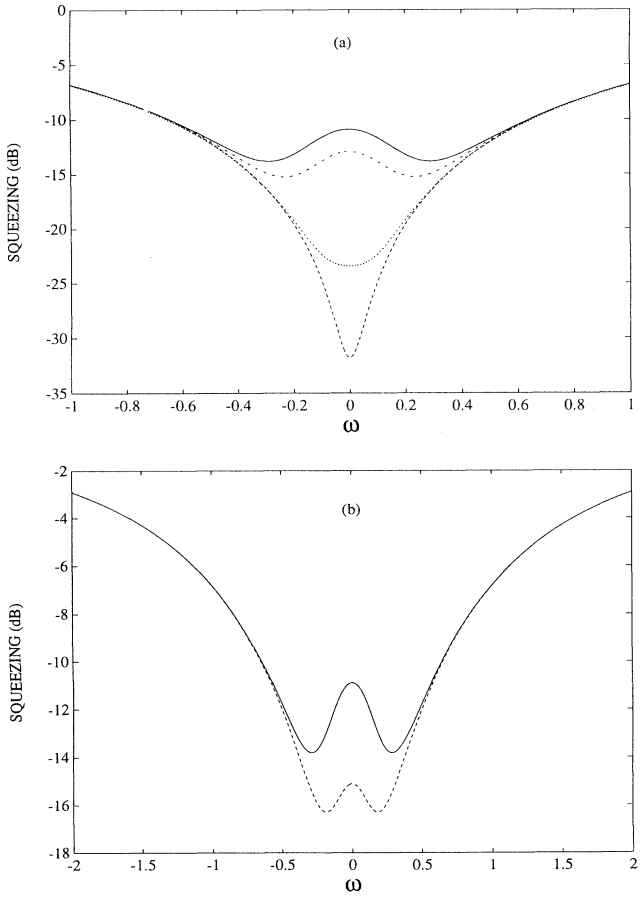


FIG. 11. Spectrum of squeezing at 95% of threshold ($p=0.95$), $\gamma=0.1$, for (a) $n_{\rm th}=600$ (solid line), $10^3$ (dash-dotted line), $10^4$ (dotted line), and linearized (dashed line), and (b) $n_{\rm th}=600$ for polarized pump mode (solid line) and unpolarized pump mode (dashed line).

dynamics is currently being pursued and the quantum limit is certainly attainable. The system-size effects we discuss are likely to be observed in Josephson-junction parametric amplifiers because of their large intrinsic nonlinearity [9]. The possibility of generating coherent-state superpositions in the quantum regime was suggested by Wolinsky and Carmichael [7]. However, a careful inspection of the homodyne detection of the OPO output by Reid and Yurke [7] reveals the superposition is absent, at least in the steady state and adiabatic limit. This still leaves open the possibility in the nonadiabatic regime. More detailed studies of the quantum limit and system-size scaling will be reported in future work.


## ACKNOWLEDGMENTS

This work was supported in part by a NATO travel grant. One of us (S.S.) would also like to acknowledge support from the U.K. Science and Engineering Research Council.


## APPENDIX A: WICK'S THEOREM

We refer to Refs. [20,21,24] for discussion of Wick's theorem. In its most familiar form, Wick's theorem arises in connection with the interaction-picture expansion of the $S$ matrix, in which annihilation and creation operators have a simple $\exp(\mp i\omega t)$ time dependence. Since the average with respect to the ground state of a normal product vanishes, and the two-time commutator of interaction picture operators is a $c$ number, it follows that (for Bose annihilation and creation operators)

$$\begin{aligned}\langle T(ABCD\cdots XYZ)\rangle &= \langle T(AB)\rangle\langle T(CD)\rangle\cdots\langle T(YZ)\rangle \\ &\quad +\langle T(AC)\rangle\langle T(BD)\rangle\cdots\langle T(YZ)\rangle+\cdots ,\end{aligned} \tag{A1}$$

the average decomposes into sums of products of all possible contractions. The diagrammatic representation and Feynman rules then follow.

In our application to dissipative nonequilibrium situations, the time ordering is replaced by path ordering [11]. To establish the usual lemmas [24] on which a path-ordered version of Wick's theorem depends, it is necessary to consider the time evolution of operators in the interaction picture. To establish this we start from a Hamiltonian theory of system and reservoir and their coupling in the Schrödinger picture [8]. First perform unitary transformations to the rotating frame and vacuum picture to remove free evolution and the classical mean-field averages, respectively. Then split the Hamiltonian into two parts, $V=H_1+H_2$, as defined in Eq. (2.3), and $H_0(t)$, the residual, which contains the system-reservoir couplings. The interaction picture is then defined so that operators and states evolve according to the interaction-picture representations of $H_0(t)$ and $V$, respectively. At this stage the Markov approximation is made on the interaction-picture equations of motion, resulting in the quantum Langevin equation for the damped harmonic oscillator [20],

$$\frac{d\hat{a}_k}{dt}=-\gamma_k\hat{a}_k(t)-\sqrt{2\gamma_k}\hat{a}_{k,\mathrm{in}}(t) . \tag{A2}$$

We assume that the cavity input is a vacuum state, representing a zero-temperature heat bath coupled to the cavity mirror, and that the system was in the vacuum state in the distant past. One can show that normally ordered averages of $\hat{a}_k(t)$ and $\hat{a}_k^\dagger(t')$, with respect to the vacuum state vanish, and that their commutator is a $c$ number,

$$[\hat{a}_k(t),\hat{a}_k^\dagger(t')]=\exp\{-\gamma_k|t-t'|\}\delta_{kk'} .$$

This is sufficient to establish the path-ordered version of Wick's theorem necessary for the application here, namely,

$$\begin{aligned}\langle T_C(ABCD\cdots XYZ)\rangle &= \langle T_C(AB)\rangle\langle T_C(CD)\rangle\cdots\langle T_C(YZ)\rangle \\ &\quad +\langle T_C(AC)\rangle\langle T_C(BD)\rangle\cdots\langle T_C(YZ)\rangle+\cdots .\end{aligned} \tag{A3}$$

## APPENDIX B: GENERAL RELATIONS AMONG MANY-BODY FUNCTIONS

We list some general relations that are useful in the analysis and implementation of the theory. As these relations are true for both modes we suppress the mode index in the formulas.

$$D^{-+}(t_1,t_2)+D^{+-}(t_1,t_2)=D^{--}(t_1,t_2)+D^{++}(t_1,t_2) , \tag{B1}$$

$$D^{++}(t_1,t_2)=-(D^{--}(t_2,t_1))^* , \tag{B2}$$

$$\begin{aligned}D^{-+}(t_1,t_2)&=-(D^{-+}(t_2,t_1))^* ,\\ D^{+-}(t_1,t_2)&=-(D^{+-}(t_2,t_1))^* .\end{aligned} \tag{B3}$$

In frequency space, we have similarly

$$D^{-+}(\omega)+D^{+-}(\omega)=D^{--}(\omega)+D^{++}(\omega) , \tag{B4}$$

$$D^{++}(\omega)=-(D^{--}(\omega))^* , \tag{B5}$$

$$\begin{aligned}D^{-+}(\omega)&=-(D^{-+}(\omega))^* ,\\ D^{+-}(\omega)&=-(D^{+-}(\omega))^* .\end{aligned} \tag{B6}$$

Note that (B6) implies $D^{-+}(\omega)$ and $D^{+-}(\omega)$ are pure imaginary. Furthermore, the polarization matrices $\underline{\Pi}_k$ $(k=1,2)$, introduced in the text, can be shown to satisfy the relations

$$\Pi_k^{++}(\omega)+\Pi_k^{--}(\omega)+\Pi_k^{+-}(\omega)+\Pi_k^{-+}(\omega)=0 . \tag{B7}$$

[1] See the special feature editions J. Mod. Opt. **34** (6) (1987); J. Opt. Soc. Am. B **4** (10) (1987).
[2] M. J. Collett and D. F. Walls, Phys. Rev. A **32**, 2887 (1985).
[3] G. Rempe, R. J. Thompson, R. J. Brcha, W. D. Lee, and H. J. Kimble, Phys. Rev. Lett. **67**, 1727 (1991); R. J. Thompson, G. Rempe, and H. J. Kimble, *ibid.* **67**, 1132 (1992).
[4] W. J. Kozlovsky, C. D. Nabors, and R. L. Byer, IEEE J. Quantum Electron. **24**, 913 (1988).
[5] G. Rempe, R. J. Thompson, H. J. Kimble, and R. Lalezari, Opt. Lett. **17**, 363 (1992).
[6] R. Graham and H. Haken, Z. Phys. **210**, 276 (1968); R. Graham, in *Quantum Statistics in Optics and Solid-State Physics,* edited by G. Hohler, Springer Tracts in Modern Physics Vol. 66 (Springer, New York, 1973), p. 1; P. D. Drummond, K. J. McNeil, and D. F. Walls, Opt. Acta **28**, 211 (1981); D. F. Walls and G. J. Milburn, in *Quantum Optics, Experimental Gravity and Measurement Theory,* edited by P. Meystre and M. O. Scully (Plenum, New York, 1983), p. 209; F. Kartner, R. Schack, and A. Schenzle, J. Mod. Opt. **39**, 917 (1992).
[7] M. Wolinsky and H. J. Carmichael, Phys. Rev. Lett. **60**, 1836 (1988); M. D. Reid and B. Yurke, Phys. Rev. A **46**, 4131 (1992); P. Kinsler and P. D. Drummond, Phys. Rev. Lett. **64**, 236 (1990); Phys. Rev. A **43**, 6194 (1991).
[8] P. D. Drummond, K. J. McNeil, and D. F. Walls, Opt. Acta **27**, 321 (1980).
[9] B. Yurke, L. R. Corruccini, P. G. Kaminsky, L. W. Rupp, A. D. Smith, A. H. Silver, R. W. Simon, and E. A. Whittaker, Phys. Rev. A **39**, 2519 (1989).
[10] J. Schwinger, J. Math. Phys. **2**, 407 (1961).
[11] L. V. Keldysh, Zh. Eksp. Teor. Fiz. **47**, 1515 (1964) [Sov. Phys. JETP **20**, 1018 (1965)].
[12] V. Korenman, Ann. Phys. (N.Y.) **39**, 72 (1966); Phys. Rev. **154**, 1233 (1967).
[13] E. M. Lifshitz and L. P. Pitaevskii, *Physical Kinetics,* Course of Theoretical Physics Vol. 10 (Pergamon, Oxford, 1981).
[14] H. R. Zaidi, Can. J. Phys. **66**, 164 (1988); **66**, 854 (1988).
[15] M. Dorfle and A. Schenzle, Z. Phys. B **65**, 113 (1986); I. J. D. Craig and K. J. McNeil, Phys. Rev. A **39**, 6267 (1989); A. M. Smith and C. W. Gardiner, *ibid.* **39**, 3511 (1989); K. J. McNeil and I. J. D. Craig, *ibid.* **41**, 4009 (1990).
[16] R. Landauer, J. Appl. Phys. **33**, 2209 (1962); R. Landauer and J. Woo, IEEE J. Quantum Electron. **7**, 435 (1971).
[17] R. G. Smith, in *Lasers: A Series of Advances,* edited by A. K. Levine and A. De Maria (Marcel Dekker, New York, 1976), Vol. 4.
[18] R. L. Byer, in *Quantum Electronics: A Treatise,* edited by H. Rabin and C. L. Tang (Academic, New York, 1975), Vol. 1, Part B, p. 587.
[19] J. Schwinger, Proc. Natl. Acad. Sci. USA **37**, 452 (1951).
[20] C. W. Gardiner and M. J. Collett, Phys. Rev. A **31**, 3761 (1985).
[21] A. A. Abrikosov, L. P. Gor'kov, and I. E. Dzyaloshinski, *Methods of Quantum Field Theory in Statistical Physics* (Dover, New York, 1963).
[22] L. P. Gor'kov, Zh. Eksp. Teor. Fiz. **34**, 735 (1958) [Sov. Phys. JETP **7**, 505 (1958)]; E. M. Lifshitz and L. P. Pitaevskii, *Statistical Physics, Part 2,* Course of Theoretical Physics Vol. 9 (Pergamon, Oxford, 1981); G. C. Wick, Phys. Rev. **80**, 268 (1950).
[23] P. Kurz, R. Paschotta, K. Fiedler, A. Sizmann, G. Leuchs, and J. Mlynek, Appl. Phys. B **55**, 216 (1992).
[24] W. H. Louisell, *Quantum Statistical Properties of Radiation* (Wiley, New York, 1973).